THE JOURNAL OF PHYSICAL CHEMISTRY C

Article

pubs.acs.org/JPCC

Using Heterodyne-Detected Electronic Sum Frequency Generation To Probe the Electronic Structure of Buried Interfaces

Aaron P. Moon,[†] Ravindra Pandey,[†,‡] Jon A. Bender, Daniel E. Cotton, Benny A. Renard, and Sean T. Roberts*

Department of Chemistry, The University of Texas at Austin, Austin, Texas 78712-1224, United States

Supporting Information

ABSTRACT: Organic semiconductors (OSCs) are attractive optoelectronic materials due to their high extinction coefficients, processing advantages, and ability to display unique phenomena such as singlet exciton fission. However, employing OSCs as active electronic components remains challenging, as this necessitates forming junctions between OSCs and other materials. Such junctions can distort the OSC's electronic properties, complicating the transfer of energy and charge across them. To investigate these junctions, our group has employed an interface-selective technique, electronic sum frequency generation spectroscopy (ESFG), yet one complication in applying ESFG to thin OSC films is they necessarily have two interfaces that can each produce signals. In a conventional ESFG measurement, information regarding the phase of the ESFG signal is lost. However, this information can be recovered with heterodyne detection (HD) techniques. Here, we present experiments and model calculations that illustrate some key advantages offered by HD-ESFG over conventional ESFG measurements for the study of OSC films. Specifically, we report HD-ESFG spectra of *N*,*N*′-dimethyl-3,4,9,10-perylenedicarboximide (C1-PDI) thin films that have been grown on SiO_2. To implement these measurements, we have constructed an HD-ESFG spectrometer that uses common path optics to maintain a high degree of phase stability over multiple hours. We find that not only does HD-ESFG offer increased sensitivity to weak features in ESFG spectra, but the phase information included in these measurements aids in selectively isolating signals that arise from a specific film interface. Interestingly, we find that resonances in HD-ESFG spectra of C1-PDI are significantly shifted from those in linear absorption spectra of bulk C1-PDI films, suggesting that the intermolecular packing of molecules at film interfaces differs from the bulk.

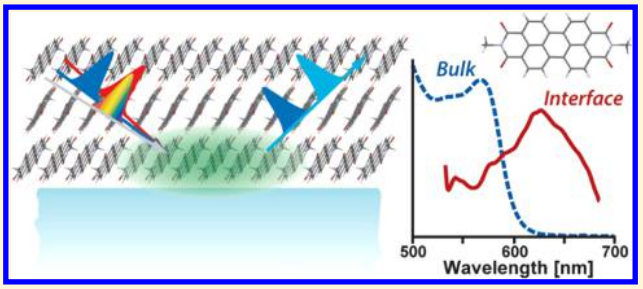

1. INTRODUCTION

Over the past decade, there has been growing interest in the use of small-molecule organic semiconductors (OSCs) to increase the efficiency of existing photovoltaic technologies. One advantage OSCs provide over conventional semiconductors is the ability to undergo a process called singlet fission (SF), a high-energy photon downconversion process that has been demonstrated to occur with robust, high efficiency in a number of OSCs.[1−13] SF is a process through which a photoexcited spin-singlet state of a molecule or molecular crystal relaxes into two separate spin-triplet excited states. This process can occur quickly and with high efficiency provided the singlet state has roughly twice the energy of the triplet state of the system, owing to total spin conservation. By combining a material capable of SF with existing solar technologies, it may be possible to improve their power conversion efficiency. When an inorganic semiconductor (ISC) absorbs a photon with a frequency greater than the transition of its intrinsic band gap, the excess energy is thermalized into the crystal lattice as the carriers relax to the band edge. This process accounts for a significant amount of the energy loss in solar cells and is a major contributing factor to the Shockley−Queisser limit for a single-junction solar cell.[14] By incorporation of a SF-capable OSC on top of a traditional ISC solar cell, high-energy photons can be converted to pairs of lower-energy triplet excitons that are close in energy to the band gap of the ISC, reducing thermalization losses. The resulting triplet excitons can then be transferred across the OSC/ISC interface for charge separation and current generation in the ISC, providing two pairs of charge carriers for each high-energy photon absorbed in the OSC layer.[15−17]

While this would be an effective method to improve device performance, the mechanism of energy transfer from the OSC to the ISC remains an active topic of research. Although efficient bidirectional triplet transfer has been observed between semiconductor quantum dots and SF-capable molecules, such as anthracene, tetracene, and pentacene,[18−21] triplet energy transfer between tetracene and bulk silicon is inefficient despite energetic matching of tetracene's triplet energy to silicon's band gap.[22,23] The details regarding why triplet transfer is inhibited in the latter are poorly understood and may reflect band narrowing at the tetracene/silicon

Received: June 5, 2017
Revised: July 27, 2017
Published: August 5, 2017

DOI: 10.1021/acs.jpcc.7b05514
J. Phys. Chem. C 2017, 121, 18653−18664

interface[24] or poor spatial overlap of tetracene's π-system and the silicon surface,[25] among other effects.

To construct a detailed understanding of energy transfer between OSC thin films and bulk ISCs, there is a need to characterize the electronic density of states (DoS) of the junction formed between them. This DoS is expected to be sensitive to the manner in which OSC molecules pack at the buried surface,[26−29] as this can alter the extent of dipolar and charge-transfer coupling between nearby OSC molecules,[30−32] as well as their degree of orbital overlap with the underlying ISC surface. As such, a technique that can measure the arrangement of molecules at a buried OSC/ISC junction as well as their electronic structure can substantially aid in building a physical picture for how energy and charge move across these junctions. Toward this end, our research group has worked to develop electronic sum frequency generation (ESFG) spectroscopy as a method to examine the energetic landscape of inaccessible interfaces in semiconductor devices.[33]

ESFG is an optical probe technique analogous to surface specific linear absorption, making it ideal to study the buried DoS in organic thin films. In an ESFG measurement, two pulses of light interrogate a sample: a white light supercontinuum (WL) and a spectrally narrow upconversion pulse.[34,35] When these two pulses are overlapped in time and space within a sample, each spectral component of the WL can coherently mix with the upconversion pulse, generating an ESFG field at their sum frequency that can be spectrally dispersed and collected by use of a charge-coupled device (CCD). Electronic resonance between molecules within a sample and frequency components of the WL can strongly enhance this mixing. As the frequency of the upconversion field is known, each spectral component of the ESFG field can be mapped onto the frequency component of the WL field that led to its generation, thereby making an ESFG spectrum analogous to a sample's linear absorption spectrum. Importantly, however, due to cancelation between back-propagating and forward-propagating fields, under the electric dipole approximation, ESFG is incapable of being generated by materials that possess inversion symmetry.[36] As buried interfaces naturally lack such symmetry, ESFG can selectively probe the electronic DoS of molecules at these critical junctions.[37,38] By measuring how the polarization of the ESFG field depends on that of the WL and upconversion fields, information regarding the orientation of molecules at a buried surface can be obtained.[33,39,40] In addition, as ESFG measurements commonly employ fields with femtosecond pulse durations, they can readily serve as a kinetic probe of excited electronic dynamics at an OSC interface.[26,41,42]

However, while ESFG is a useful probe of interfacial electronic structure and morphology, measuring and interpreting ESFG signals from OSC thin films presents a few specific challenges. First, as ESFG is produced by only a small number of monolayers near an interface, the signals generated in this technique are inherently weak, leading to the need for long collection times to achieve a reliable signal-to-noise ratio. Second, though ESFG signals are intrinsically interface-specific, each interface within a sample can produce its own ESFG signal. This can complicate the interpretation of ESFG signals from OSC thin films as they have at least two active interfaces: a buried interface, where charge and energy transfer take place, and an outer air-exposed interface. Signals emitted by these two interfaces can interfere with each other, making the extraction of information exclusive to the buried interface difficult.[33,43−46] Moreover, even if separating the contributions from the outer and buried interfaces is possible, the experiment may be more sensitive to the outer interface, as the WL field can be strongly attenuated as it passes through an optically thick sample to a buried interface. Finally, the signal measured in an ESFG experiment as described above contains no information related to the sign of the induced polarization between an OSC and its underlying substrate. This reflects that a measurement of the ESFG field emitted by a sample, $\vec{E}_{\mathrm{samp}}$, by a CCD measures the field's intensity rather than its amplitude and phase:

$$I_{\mathrm{ESFG}} \propto |\vec{E}_{\mathrm{samp}}|^2 \propto |\chi^{(2)}|^2 \tag{1}$$

In eq 1, the intensity of the measured ESFG signal is proportional to the square of $\chi^{(2)}$, the second-order nonlinear susceptibility of an interface whose sign reports on the direction of the induced polarization between an OSC and its substrate.[47−49] When only the intensity of an emitted ESFG field is measured, information regarding the sign of the induced polarization giving rise to the ESFG field is lost. However, knowledge of such information is critical, as it can describe the extent to which OSC molecules polarize in response to being placed into contact with a high-dielectric ISC, which can lead to band bending of both materials at their junction.[49,50] We refer to ESFG signals measured in this manner as direct ESFG.

To overcome the shortcomings of direct ESFG, our group has implemented a heterodyne detection (HD) scheme for recording ESFG spectra. In contrast to a direct ESFG measurement, where the WL and upconversion beams simply generate an ESFG field from a sample, in an HD-ESFG experiment these beams are also used to create a reference field, referred to as a local oscillator (LO), by focusing them onto a noncentrosymmetric material that produces a strong, nonresonant ESFG signal. The signal field produced by a sample is then spatially overlapped with that of the LO, $\vec{E}_{\mathrm{LO}}$, and spectrally detected.[47−49,51−60] Interference between the strong LO field and weaker signal field gives rise to a cross term that oscillates at the phase difference between these two fields:[48]

$$\begin{aligned} I_{\mathrm{HD\text{-}ESFG}} &\propto |\vec{E}_{\mathrm{samp}}\vec{E}_{\mathrm{LO}}|^2 \\ &= |\vec{E}_{\mathrm{samp}}|^2 + |\vec{E}_{\mathrm{LO}}|^2 + 2|\vec{E}_{\mathrm{samp}}||\vec{E}_{\mathrm{LO}}|\cos(\phi_{\mathrm{samp}} - \phi_{\mathrm{LO}}) \end{aligned} \tag{2}$$

Fourier filtering of the data can selectively isolate this cross term. If the LO phase and amplitude are known, the phase and amplitude of the ESFG signal can be directly determined from the cross term. Importantly, as we demonstrate below, the retrieval of the ESFG signal phase from a thin OSC film provides an additional constraint that aids in separating signal contributions that arise from the film's outer and buried interfaces. Moreover, as the cross term scales linearly in both the ESFG signal field and the LO field, the LO can amplify weak ESFG fields, reducing the data collection times needed to boost these signals above the shot noise limit.

Here, we employ HD-ESFG to study the buried interfacial structure of thin films of *N*,*N*′-dimethyl-3,4,9,10-perylenedicarboximide (C1-PDI) that have been vapor-deposited on fused quartz. C1-PDI is a member of the larger family of perylenediimide molecules that have been examined as promising candidates for the development of SF sensitizers for photovoltaic cells and other light-harvesting schemes.[4,7,61,62] Below, we describe a simplistic scheme for constructing an HD-ESFG spectrometer that makes use of common path optics to minimize phase jitter between the sample and LO fields during

DOI: 10.1021/acs.jpcc.7b05514
J. Phys. Chem. C 2017, 121, 18653−18664

measurements. This spectrometer shows minimal drift over multiple hours, and the scheme for its implementation should be readily amenable to integration with existing ESFG spectrometers. We also show that HD-ESFG aids in the detection of weak ESFG features and that the inclusion of spectral phase in an optical interference model allows for a more accurate reconstruction of the $\chi^{(2)}$ of a buried OSC interface. Interestingly, we find that HD-ESFG spectra measured for C1-PDI thin films are significantly red-shifted relative to bulk absorption spectra, suggesting that C1-PDI molecules adopt a packing structure at the SiO_2 interface that is modified relative to the crystalline arrangements they adopt in the bulk regions of these films. This result highlights the sensitivity of HD-ESFG to the electronic DoS of buried OSC interfaces and suggests its future utility in studying the extraction of triplet excitons from SF-capable OSCs.

2. EXPERIMENTAL METHODS AND SAMPLE PREPARATION

2.1. Preparation and Characterization of C1-PDI Films. C1-PDI was purchased from Sigma–Aldrich (98% purity) and used as received. Uniform thickness C1-PDI films were vapor-deposited onto fused quartz (SiO_2) plates (GM Associates, $^1/_{16}$-in. thickness) by use of an ultra-high-vacuum (UHV) thermal deposition chamber (AMOD PVD system, Ångström Engineering) with a base pressure of $\sim 5 \times 10^{-7}$ Torr and a deposition rate of 1 Å/s. Substrates were sonicated in chloroform, toluene, and 2-propanol, in that order, and then rinsed with methanol and dried under N_2 prior to thermal deposition. Variable-angle spectral ellipsometry (M-2000, J. A. Woollam) was used to determine the thickness of vapor-deposited films as well as their optical constants. Samples for these measurements consisted of films that were grown on top of n-type Si(100) substrates with a native oxide layer. These films were produced concomitantly with films deposited on SiO_2 for ESFG measurements to ensure thickness uniformity for both samples. Si substrates were cleaned by a procedure identical to that for SiO_2 plates prior to film deposition. All ESFG results presented in this paper were measured for a C1-PDI film found to have a thickness of 52 nm via ellipsometry. Transmission and reflection spectra of sample films were recorded on a UV–vis spectrometer with an integrating sphere attachment (Shimadzu UV-2600). Absorption spectra that appear in Figures 4 and 7 have been corrected to account for reflection and scattering losses.

2.2. Heterodyne-Detected Electronic Sum Frequency Generation Spectroscopic Measurements. Our experimental setup for HD-ESFG measurements (Figure 1) was built as an addition to our spectrometer for direct ESFG spectra, described in detail elsewhere.[33] Briefly, a femtosecond Ti–sapphire regenerative amplifier (Coherent Legend Duo Elite, 3 kHz, 4.5 mJ) was used to generate a 90 fs pulse centered at 804 nm with a bandwidth of 160 cm^{-1} (full width at half-maximum, fwhm). A small portion of the amplifier output (0.1 mJ) was focused into a water flow cell to generate a white light supercontinuum (WL). The WL was collimated and passed through a pair of spectral filters to reduce its bandwidth to a spectral range extending from 450 to 800 nm. A second portion of the amplifier was used as the narrow-band upconversion pulse. Typical pulse energies for the filtered WL and upconversion pulses were 2 μJ and 1 μJ, respectively. We chose these powers as we found that the ESFG signal from a C1-PDI film displayed no significant changes over the course of 30 min when irradiated at this power level (Supporting Information, Figure S5), suggesting that the beams inflict no photodamage to the film.

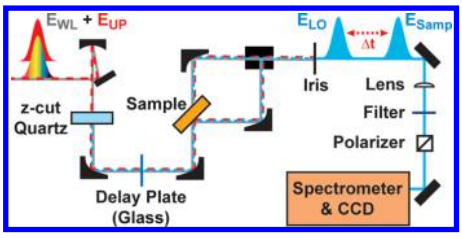

Figure 1. Experimental layout for HD-ESFG measurements. The LO field is produced by focusing the WL and upconversion fields into a z-cut quartz piece ahead of a sample.

Prior to the sample, the upconversion and WL beams were focused by use of a 15 cm focal length concave mirror in a noncollinear geometry into a piece of z-cut quartz with a thickness of 20 μm (Newlight Photonics). As z-cut quartz is a noncentrosymmetric material, it generates a nonresonant, bulk-allowed ESFG signal that serves as the LO field for HD-ESFG measurements. Following the quartz piece, the transmitted LO, WL, and upconversion fields were collimated with a 90° off-axis parabolic mirror (A50331AL, Newport). Following beam collimation, there was enough spatial separation between the three beams to introduce a silica microscope coverslip with a thickness of 145 μm (Fischerbrand) into the path of the LO exclusively. This coverslip acts as a delay plate that slows the time of arrival of the LO at the sample relative to the WL and upconversion fields. Following the delay plate, all three fields are focused by use of a second 90° off-axis parabolic mirror onto a sample film oriented at 45° with respect to the plane of the incident beams. Here, the WL and upconversion fields drive the generation of an ESFG signal field from the sample that, due to phase-matching considerations, is emitted in a direction collinear with the LO. Following the sample, a third 90° off-axis parabolic mirror collimates both the LO and signal fields reflected or transmitted by the sample. These fields are then passed through an iris to remove the upconversion and WL fields, followed by a spectral filter (UG11, Schott) to remove any scattered upconversion or WL photons that travel collinearly with the two ESFG fields. Prior to being focused onto the entrance slit of a spectrometer (Acton Spectra Pro SP2500), the ESFG signal and LO fields were passed through a polarizer, to select either their P or S components, and a waveplate that rotates the polarization of these fields back to S-polarization due to the increased sensitivity of our spectrometer to S-polarized light. The spectrometer used a 600 groove/mm grating blazed at 300 nm (Richardson Gratings) to spectrally disperse the signal onto a liquid nitrogen-cooled CCD camera (PyLoN 2KBUV, Princeton Instruments).

Each HD-ESFG spectrum reported here was collected for PPP polarization, where PPP refers to, in order, the polarization of the ESFG signal, upconversion, and WL fields. To collect direct ESFG spectra for comparison to HD-ESFG data, the LO was removed ahead of the sample by placing a small beam block following the delay plate. Analogously, the spectrum of the LO was recorded by using an iris to block the WL and upconversion fields before they reached the sample. A background was collected for each scan by delaying the upconversion field by 100 ps with respect to the WL field and

DOI: 10.1021/acs.jpcc.7b05514
J. Phys. Chem. C 2017, 121, 18653–18664

collecting a spectrum for the same integration time used to measure ESFG spectra.

As the WL field passes through a significant amount of dispersive material following its generation, it is chirped in time with approximately a 1.4 ps separation between its reddest and bluest frequency components. This time separation is roughly an order of magnitude longer than the pulse width of the upconversion field, ∼100 fs. As ESFG is generated only when the upconversion and WL beams interact with a sample at the same time, to ensure the upconversion field has the opportunity to mix with each frequency component of the WL pulse, ESFG spectra were collected by scanning the time delay between the WL and upconversion fields by use of a computer-controlled delay stage (Newport XMS50). Unless otherwise noted, each ESFG spectrum in this report represents the sum of a set of measurements wherein the time delay between the WL and upconversion fields was scanned over a range of 1.5 ps in 100 fs steps.

Figure 2A displays the HD-ESFG spectrum of a GaAs(110) wafer recorded by the methodology outlined above. Similar to

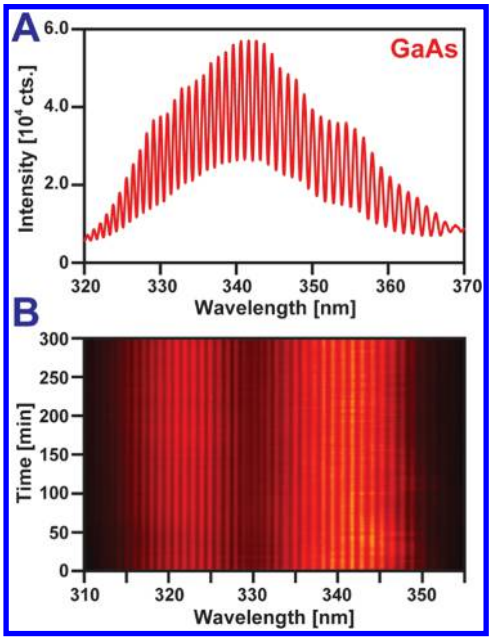

Figure 2. (A) HD-ESFG signal recorded for a GaAs(110) wafer. (B) HD-ESFG spectra of a z-cut quartz plate placed in the sample position, measured every 30 s for 5 h. Spectral fringes show minimal evidence of motion, highlighting the phase stability of our experimental layout.

z-cut quartz, GaAs is a noncentrosymmetric material and hence generates an intense reflected ESFG signal whose spectral line shape largely follows that of the WL pulse.[42,48] Due to interference between the ESFG fields emitted by the quartz and GaAs pieces, spectral fringes can be observed in the collected HD-ESFG spectrum. The spacing between these fringes reflects the phase difference between the LO and GaAs signal fields, which can be adjusted by controlling the time separation between these fields via the thickness and tilt of the delay plate. As the amplitude of the GaAs ESFG field is comparable to that of the quartz-generated LO, the oscillations that result from the interference between these fields approach the theoretical limit of 50% for two equal-amplitude fields.

One concern in the construction of a spectrometer for optical heterodyne measurements is minimizing path-length fluctuations between the LO and signal fields that can randomize the phase of the heterodyne signal produced by their interference. Such fluctuations are of particular concern when detecting interferograms in the ultraviolet spectral range, as a path-length shift on the order of half the wavelength of the signal field will cause the sign of the detected interferogram to flip. Thus, for the signals reported here, path-length fluctuations of ∼170 nm between the signal and LO during data collection will cause the HD-ESFG signal produced by their interference to average to zero.

To ensure that the distance separating the LO and ESFG signal fields generated by our HD-ESFG setup remain fixed throughout an experiment, we have used common path optics to propagate the LO, WL, upconversion, and signal fields following optics used to filter the WL (Figure 1). Thus, any fluctuations in the optical path of our spectrometer will be transferred to each of these beams, holding fixed the relative phase of the signal and LO. As an illustration of this point, in Figure 2B we plot HD-ESFG spectra of a z-cut quartz piece placed at the sample position that were taken every 30 s over the course of 5 h. Over this time span, we see that interference fringes produced between the LO and ESFG signal fields display almost no discernible drift. Comparing the first recorded spectrum to that measured after 5 h indicates a change in phase of 0.43 radians, which corresponds to a path length change of only ∼24 nm ($\sim\lambda/15$) in the relative path traveled by the LO and ESFG fields over this time. Such long-term phase stability is required for measurements that aim to detect changes in the ESFG signal intensity of a sample in response to an external stimulus, such as a time-delayed excitation pulse in transient ESFG measurements.[41,49,63−65]

3. RESULTS AND DISCUSSION

Phase-sensitive detection of ESFG fields produced by use of WL continua was previously implemented by Yamaguchi and Tahara.[48] In their setup, the WL and upconversion fields were first focused onto a sample in a reflection geometry, generating ESFG. The reflected WL, upconversion, and ESFG fields were then captured by use of a spherical mirror and refocused onto a GaAs(110) wafer to produce a LO field that was emitted in a direction collinear with the ESFG field. While this setup has been used to great effect to study the structure of liquid interfaces[66−68] and monolayer films,[48] using it to study buried interfaces of thin OSC films presents some significant challenges. First, OSC thin films are known to produce ESFG signals from each of their interfaces that interfere at a detector. The signal from a specific interface of interest can be isolated by measuring spectra of films of different thicknesses or by varying the angle of incidence of the WL and upconversion fields.[33,43−45] However, as many OSCs are highly absorbing, they can strongly modify the spectrum of the reflected WL field used to generate a LO in the scheme of Yamaguchi and Tahara.[48] This creates a complication when either OSC film thickness or sample tilt is altered with respect to the WL and upconversion fields, as this can modify the spectrum of the LO used for HD-ESFG detection. Second, producing the LO by use of fields reflected from a sample's surface creates a practical issue, as the sample itself acts as a mirror. Slight changes in the tilt of a sample when exchanging one for another can alter the steering of beams onto a GaAs wafer placed after the sample, thereby affecting the efficiency of LO generation. Finally, GaAs itself is highly absorbing in the ultraviolet spectral range. As the signal emitted by a sample needs to be reflected off a GaAs

DOI: 10.1021/acs.jpcc.7b05514
J. Phys. Chem. C 2017, 121, 18653−18664

surface in this scheme, absorption of the signal by GaAs can negate some of the signal-to-noise gains expected from heterodyne detection.

To address the issues noted above, our experimental layout for HD-ESFG generates the LO by use of a transmissive z-cut quartz piece placed ahead of the sample. This layout is similar to that recently implemented by Inoue et al.[56] and Vanselous and Petersen[58] for measuring heterodyne-detected vibrational sum frequency generation, but to our knowledge has yet to be adapted to the measurement of broadband HD-ESFG spectra employing a WL continuum. Generating the LO prior to the ESFG signal from a sample carries the distinct advantage that the LO's spectral profile is no longer tied to the sample film's reflectivity, ensuring that each sample investigated in our layout experiences an identical LO field. Moreover, by using a transmissive geometry to generate the LO, we simplify the alignment of our HD-ESFG spectrometer, as the substrate that produces the LO is no longer used as a mirror. This geometry allows us to easily change between detecting ESFG signals reflected or transmitted from a sample without the need to reoptimize generation of the LO.

Figure 3A plots the spectrum of the LO field produced by overlapping the WL and upconversion fields in a 20 μm z-cut quartz crystal alongside the spectrum of the ESFG field created by focusing these beams reflectively onto a GaAs substrate. The spectrum of the signal produced by GaAs largely follows that of the WL field, and its spectral extent is ultimately limited in our setup by a bandpass filter placed after the sample that removes residual scattered light from the WL field. As the LO produced by z-cut quartz is created nonresonantly, it too should display a spectrum that tracks that of the WL field. However, the LO's spectrum is instead highly structured, showing a series of narrower peaks that resemble the WL spectrum convolved with a $\sinh^2(\omega)$ function. This narrowed spectrum represents one disadvantage of using a transmissive geometry to produce the LO, as the dispersion of the z-cut quartz crystal leads to temporal walkoff between the ESFG field and the WL and upconversion fields that generate it as they propagate through the crystal. This leads to a phase shift between ESFG fields created at different points within the crystal that can negate this field for certain wavelengths.[69] The bandwidth of the LO can be maximized by minimizing the thickness of the crystal used to produce it,[52,56] and the position of peaks within the LO spectrum can be tuned by altering the angle between it and the incident WL and upconversion fields (Figure 3B). Nevertheless, for the 20 μm z-cut crystal we employ here, we find that our LO has a bandwidth of ~2200 cm^{-1} (fwhm of central peak), which is broad enough to span the lowest energy electronic transition of C1-PDI.

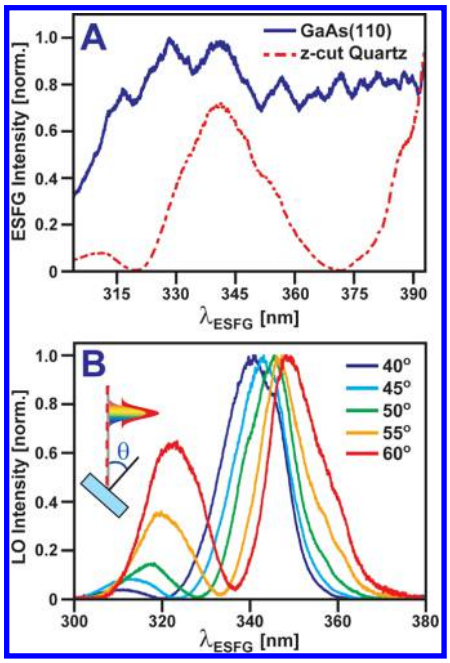

Figure 3. (A) Spectrum of the transmitted LO field created by focusing the WL and upconversion pulses into a 20 μm z-cut quartz plate (red dashed) vs. the spectrum of the reflected ESFG field produced by focusing the WL and upconversion pulses onto a GaAs(110) wafer (blue). Due to temporal walkoff within the quartz plate, the LO field is spectrally modulated. (B) Spectrum of the LO field as a function of the angle of incidence between the WL and upconversion fields. For these measurements, a 35 μm z-cut quartz plate was used in place of the 20 μm quartz plate employed for HD-ESFG.

Figure 4 plots the linear absorption spectrum of a 52 nm C1-PDI film vapor-deposited on SiO_2. When dissolved as monomers in CH_2Cl_2 solution, C1-PDI displays a prominent peak at 524 nm that corresponds to its highest occupied to lowest unoccupied molecular orbital (HOMO to LUMO) transition, along with higher-energy vibronic replicas of this transition separated by ~1410 cm^{-1}, associated with C1-PDI's ring breathing modes (Supporting Information, Figure S2). The spectrum of vapor-deposited C1-PDI distinctly differs from that of monomeric C1-PDI, displaying two broad peaks at 474 and 568 nm and a smaller shoulder at 536 nm (Figure 4). XRD and AFM data measured for our C1-PDI films (Supporting Information, Figure S3) indicate they are comprised of micrometer-sized polycrystalline grains wherein molecules are arranged into slip-stacked columns (Figure 4, inset) with neighbors separated by distances of ~3.5 Å.[70,71] This close arrangement of molecules in the solid state allows for dipolar through-space coupling between distant molecules as well as direct charge-resonance interactions between neighboring PDIs that modify their absorption spectra.[30−32]

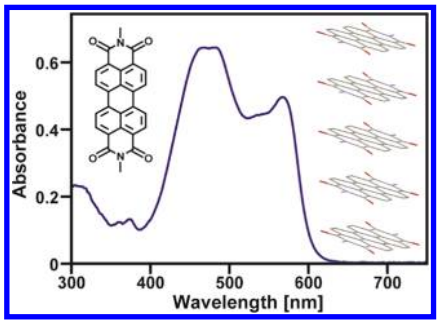

Figure 4. Linear absorption spectrum of a 52 nm C1-PDI film (structure shown in left inset). The spectrum has been corrected to account for reflection losses. C1-PDI films are comprised of crystallites with neighboring molecules arranged in a slip-stacked manner (right inset). Plotted crystal structure was taken from ref 70.

Figure 5A displays a contour plot showing HD-ESFG spectra measured for a 52 nm C1-PDI film as a function of the time delay between WL and upconversion fields. As the delay between these fields is scanned, the envelope of the response undergoes a pronounced frequency shift due to the chirp in the

DOI: 10.1021/acs.jpcc.7b05514
J. Phys. Chem. C 2017, 121, 18653−18664

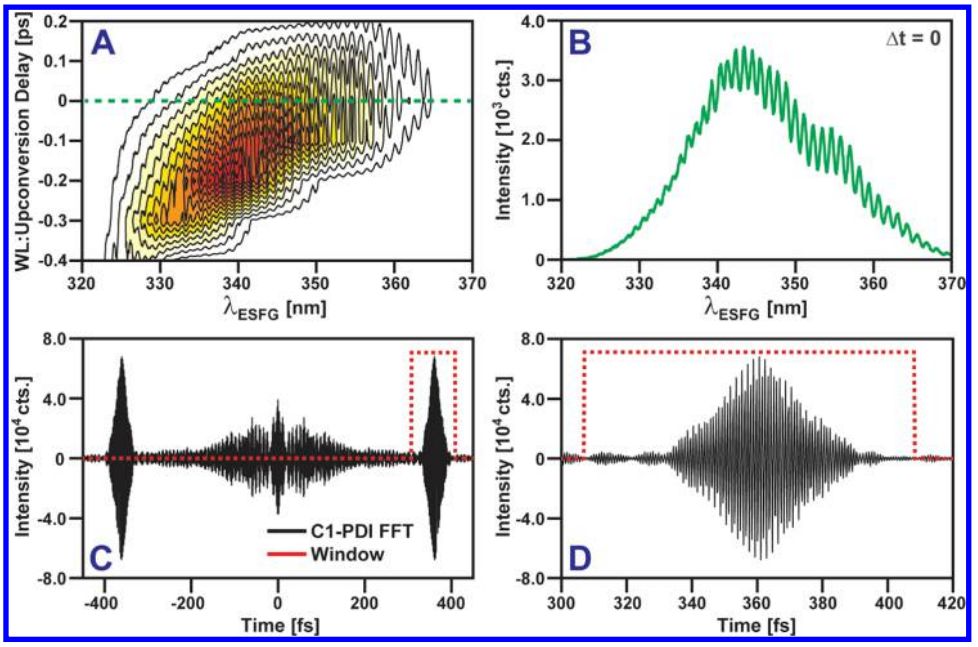

Figure 5. (A) HD-ESFG signal of 52 nm C1-PDI film on SiO_2 substrate as a function of the time delay between upconversion and WL fields. (B) Spectral slice of data in panel A, taken at the position highlighted by the dashed green line (0 ps). (C) Fast Fourier transform (FFT) of the scan shown in panel B (black) and the window used to extract the cross term at 360 fs (red). Note that the peak at t = 0 has been suppressed by subtracting the spectrum of the LO and direct ESFG signals prior to performing FFT. (D) Zoomed view of cross term and window in panel C.

WL field. Oscillations are apparent in the spectrum at each time delay, due to interference between the LO and ESFG field emitted by the C1-PDI film. These oscillations are highlighted in Figure 5B, which shows a slice through the data set in Figure 5A indicated by the dashed green line. As with any heterodyne detection scheme, care must be taken in setting the intensity of the LO relative to that of the signal emitted by a sample to ensure that the measured spectrum is not dominated by the background $|\vec{E}_{LO}|^2$ contribution. In our setup, the amplitude of the LO can be tuned via in-plane rotation of the z-cut quartz crystal. Such tunability is important as the direct ESFG signal, $|\vec{E}_{samp}|^2$, produced by a C1-PDI film is 275× weaker than that of a GaAs wafer. For the data shown in Figure 5, the LO intensity was maximally attenuated by rotation of the z-cut quartz, yielding an intensity ratio of 89 for $|\vec{E}_{LO}|^2/|\vec{E}_{samp}|^2$. Decreasing this ratio further by replacing the delay plate used to temporally separate the LO and signal with a similarly thin neutral density filter could, in principle, improve the fringe depth achieved in Figure 2B. Nevertheless, as constructed, our setup has enough flexibility to detect heterodyne signals from both strong (GaAs) and weak (C1-PDI) emitters.

Figure 5C plots the real portion of the Fourier transform of the HD-ESFG signal, which displays two intense peaks at time delays of ±360 fs as well as a broad band centered at t = 0. Looking at eq 2, it is apparent that the features at ±360 fs represent the cross terms that contain a product of the LO and sample signal field, while the band centered at t = 0 denotes the $|\vec{E}_{LO}|^2$ and $|\vec{E}_{samp}|^2$ contributions to the signal. We can isolate the cross term by applying a window function to the Fourier transform that selects one of the peaks at ±360 fs and subsequently performing an inverse Fourier transform.[48,51,55] We note that the thickness of the glass plate used to introduce a time delay between the LO and signal fields is critical to the success of this analysis scheme. If the plate is too thin, it will not introduce a significant enough timing shift to separate the cross term between the LO and signal fields from that of the $|\vec{E}_{LO}|^2$ and $|\vec{E}_{samp}|^2$ signal contributions in the temporal domain. Conversely, if the plate is too thick, it will minimize the interference between the LO and signal fields at the detector. In our implementation, we have employed a 145 μm thick glass plate that creates a delay of 360 fs between the LO and signal fields at the detector. This delay can be fine-tuned by slight alteration of the tilt of the glass plate or by replacing the plate with a pair of variable-thickness wedges.[72,73]

Fourier transform filtering of the data in Figure 5A was used to isolate the cross term between the LO and C1-PDI signal fields, $|\vec{E}_{samp}||\vec{E}_{LO}|$, whose spectrum is plotted in Figure 6A (black line). Plotted alongside this spectrum is a direct ESFG spectrum of the same C1-PDI sample film recorded without the use of a LO, $|\vec{E}_{samp}|^2$ (red line). Both sets of data were measured with a 120 s integration time, and we have processed the data in a manner such that the amplitudes of the cross term and direct ESFG signal should be comparable. As expected, the HD-ESFG spectrum is more intense than the direct signal due to the additional contribution from the LO. As the LO is not spectrally flat, this contribution skews the HD-ESFG spectrum, causing it to peak at a shorter wavelength than the direct signal. This can be corrected by dividing the cross term by the amplitude of the LO. In practice, this division is achieved by normalizing the Fourier-transformed HD-ESFG spectrum of the C1-PDI film to the spectrum resulting from a similar set of measurements performed on a GaAs(110) wafer. In so doing, we correct for not only the spectral contribution from the LO but also the spectral dependence of the WL field.

Figure 6B compares the value of $|\vec{E}_{samp}|^2$ determined by applying this normalization procedure to the HD-ESFG data with the value measured directly without the use of a LO. Similar to the HD-ESFG spectrum, the spectrum of the WL field has been deconvoluted from the directly detected ESFG signal by normalization to a similar measurement performed on

DOI: 10.1021/acs.jpcc.7b05514
J. Phys. Chem. C 2017, 121, 18653−18664

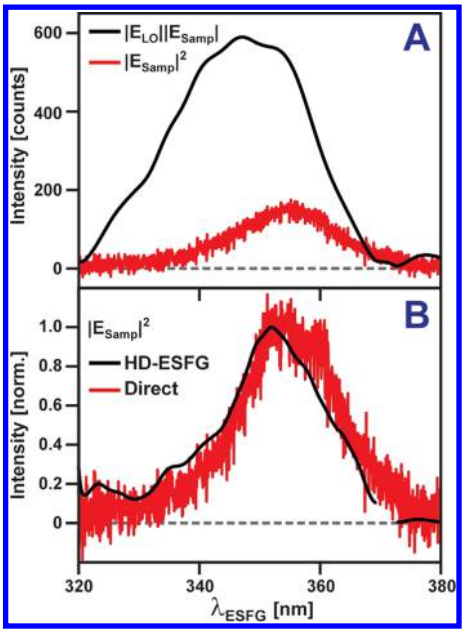

Figure 6. (A) Cross term extracted from the HD-ESFG spectrum of a 52 nm C1-PDI film on amorphous quartz (black) vs. the directed detected ESFG spectrum of the same film (red). (B) Spectra of $|\vec{E}_{samp}|^2$ extracted from HD-ESFG (black) and direct ESFG measurements (red). The gap in the spectrum derived from HD-ESFG at 370 nm results because the LO has negligible amplitude at this wavelength.

GaAs. Overall, there is quite good agreement between both sets of spectra, in terms of both the position and relative amplitude of peaks. Importantly, while both spectra display a prominent peak near 352 nm, some of the smaller bands that appear at 325, 335, and 340 nm in the HD-ESFG spectrum are obscured by detector noise in the direct ESFG spectrum. Here we see one of the advantages offered by HD-ESFG detection. In a direct ESFG measurement, two sources of noise can commonly obscure a signal: electronic noise, associated with the readout of signals from a detector, and shot noise, due to fluctuations in the intensity of the laser source. For samples that generate strong ESFG fields, electronic noise in a direct ESFG measurement can be small relative to the strength of the ESFG signal. For such signals, where laser shot noise acts as the dominant noise source, optical heterodyne detection offers no significant signal-to-noise advantage over direct detection of the signal field, as the shot noise of the signal field is simply amplified by the LO.[55,74] However, for weak spectral components of an ESFG signal that are comparable in amplitude or weaker than the electronic noise level of the detector, heterodyne detection can boost the signal amplitude above the detector's noise floor. As such, weak bands that appear at short wavelengths in the direct ESFG spectrum in Figure 6B are much more pronounced in the HD-ESFG spectrum.

As additional proof of the increased sensitivity of HD-ESFG to weak signals, in Figure S4 of the Supporting Information we compare HD-ESFG and direct ESFG spectra measured for the 52 nm C1-PDI film for different time delays between WL and upconversion fields. As this time delay increases, the temporal overlap of these fields within the C1-PDI film decreases, leading to a reduction of its ESFG signal. Interestingly, we find that, for time delays where the directly detected ESFG signal is significantly obscured by the baseline noise of the detector, the HD-ESFG signal remains clearly discernible.

While both the HD-ESFG and direct ESFG spectra in Figure 6B should overlap following the deconvolution steps above, there is a notable 2 nm shift between the peak of these spectra. One possible explanation for this shift is that it results from improved sensitivity to low-amplitude features in the HD-ESFG measurement that are obscured in direct ESFG measurements. Alternatively, this shift could result from imperfect deconvolution of the LO from the HD-ESFG spectrum. Temporal walkoff within the quartz crystal used to generate the LO limits its bandwidth and causes its amplitude to drop substantially near 373 nm. While this signal drop can, in principle, be corrected by normalizing the HD-ESFG spectrum to the LO's spectral amplitude, as is done in Figure 6B, this deconvolution assumes perfect spectral overlap between the LO and signal field emitted by a sample, which likely breaks down near regions wherein the LO displays a complicated temporal shape, as would be expected near 373 nm. Using a thinner piece of z-cut quartz to produce the LO can extend its spectral bandwidth and mitigate windowing effects imposed on HD-ESFG spectra.

In Figure 7 we compare the linear absorption spectrum of the C1-PDI film (blue dashed line) with the amplitude of the ESFG field emitted by it, $|\vec{E}_{samp}|$, as determined by HD-ESFG (red solid line). To aid in comparing these two spectra, we have plotted the ESFG data as a function of both the wavelength of the emitted ESFG field, λ_{ESFG}, and the wavelength of the WL field that drives its emission, λ_{WL}. From the data, it is clear that the film's ESFG spectrum distinctly differs from its linear absorption spectrum. While the film's lowest energy absorption band peaks at 568 nm, the ESFG spectrum is shifted to lower energy, peaking instead at λ_{WL} = 627 nm with a broad tail that extends to nearly 700 nm.

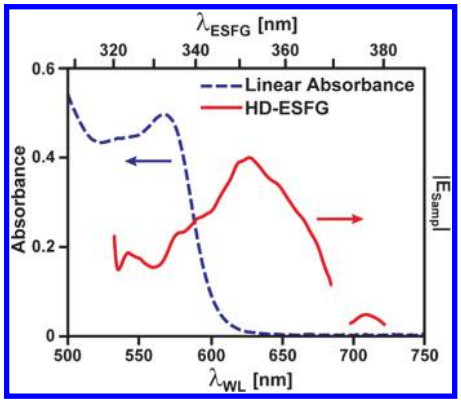

Figure 7. Comparison of the linear absorption spectrum of a C1-PDI film (blue dashed line) with its HD-ESFG field amplitude, $|\vec{E}_{samp}|^2$ (red solid line). While the lowest energy band of the C1-PDI absorption spectrum appears at 568 nm, the HD-ESFG spectrum peaks at λ_{WL} = 627 nm, suggesting a change in packing structure of the PDI film near the SiO_2/PDI interface.

One potential explanation for the prominent red shift of the ESFG spectrum is that its emission from the C1 film is driven not by resonance between spectral components of the WL field and C1-PDI's valence electronic transitions but rather by resonance between the frequencies produced by summing the WL and upconversion fields and higher-lying C1-PDI electronic states. However, in this scenario, the strength of the emitted ESFG field would be proportional to the product of

DOI: 10.1021/acs.jpcc.7b05514
J. Phys. Chem. C 2017, 121, 18653−18664

C1-PDI's one-photon and two-photon absorption cross sections at λ_{ESFG}.[75,76] As the film shows only minimal absorption in the UV spectral range (Figure 4), this scenario seems unlikely. A second hypothesis for the observed red shift of the ESFG spectrum is that molecules in the vicinity of the SiO_2 interface experience some degree of solvatochromic stabilization.[24] However, the static dielectric constant of SiO_2 is only marginally larger than that of bulk C1-PDI, which suggests this hypothesis may not fully explain the magnitude of the red shift we observe. A third explanation, which seems most likely, is that the presence of the SiO_2 layer imparts strain to C1-PDI crystallites at the junction between these materials. Strain can either expand or contract the C1-PDI lattice, leading to slight changes in the slip-stacking arrangements between molecules at the C1-PDI/SiO_2 interface. Absorption spectra of PDI molecular crystals are strongly dependent on the degree of intermolecular slip between molecules, as these arrangements dictate the strength and sign of charge-resonance coupling between neighboring molecules.[30−32] Indeed, shifts in the slip-stacking arrangements between neighboring PDI molecules on the order of a few angströms can tune the absorption maxima of PDI molecular crystals from 500 to 678 nm.[77] As such, strain-induced changes in C1-PDI's packing structure at the SiO_2 interface could explain the red shift we observe in ESFG spectra.

However, differentiating between these scenarios and others requires the HD-ESFG spectrum measured for C1-PDI to accurately report on the electronic DoS of the buried C1-PDI/SiO_2 interface. We[33] and others[43−46] have shown that sum frequency spectra of OSC thin films contain contributions from both their air-exposed and buried interfaces. At a detector, these two signals can interfere, modifying the measured ESFG spectrum. Therefore, extracting information from an ESFG spectrum necessitates first fitting the data by use of a thin-film interference model that can separate signal contributions that originate from each interface of an OSC film.[33,43] As we will show, HD-ESFG spectra allow for more accurate retrieval of $\chi^{(2)}$ of a buried OSC surface than direct ESFG measurements, as HD-ESFG measurements provide the spectral phase of the ESFG signal field. This information delivers an additional constraint that can differentiate between distinct trial $\chi^{(2)}$ line shapes that produce similar fits to direct ESFG spectra.

To test how inclusion of the spectral phase of ESFG signals influences our ability to extract $\chi^{(2)}$ of a buried OSC interface, we performed a set of model calculations where we considered a thin film of a PDI molecule related to C1-PDI, *N*,*N*′-dioctyl-3,4,9,10-perylenedicarboximide (C8-PDI), that had been deposited on an amorphous SiO_2 substrate. Each interface of the C8-PDI layer was assumed to be ESFG-active, with $\chi^{(2)}$ containing a pair of Lorentzian oscillators (see Supporting Information, Figure S6). Using this information and known optical constants of both SiO_2[78] and C8-PDI,[46] we employed an approach developed by O'Brien and Massari[43] to calculate how the ESFG field reflected by the film varies with the thickness of the C8-PDI layer. This calculation assumes an angle of incidence of 45° for each beam and a polarization combination of SPS for the ESFG, WL, and upconversion fields, respectively. For this polarization condition, only the $\chi^{(2)}_{yzy}$ component of the total $\chi^{(2)}$ tensor contributes to the ESFG response.[39,40] We then add Gaussian-distributed noise to this signal to make it more representative of experimental data. The result of this calculation is shown in the top panel of Figure 8,

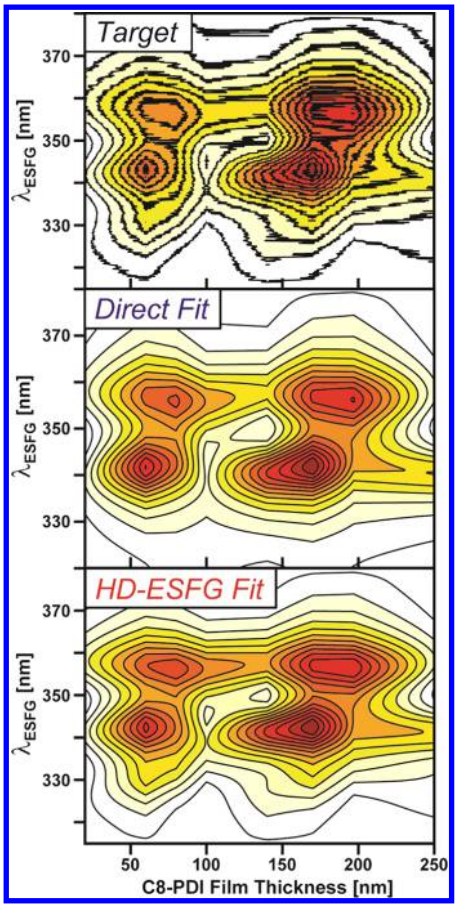

Figure 8. (Top panel) Target data set used to test the importance of including phase in a thin-film interference model for determining $\chi^{(2)}_{yzy}$ of a buried OSC interface. The plotted data show the square modulus of an ESFG field, $|\vec{E}_{samp}|^2$, as a function of film thickness. Fits to this data set that do not account for the spectral phase of the signal field (middle panel) can produce results that are nearly indistinguishable from ones that do (bottom panel).

which plots the square modulus of the ESFG field, $|\vec{E}_{samp}|^2$, as a function of film thickness. This signal corresponds to that which would be measured in a direct ESFG experiment. As the thickness of the sample film increases, the ESFG signal is observed to oscillate in amplitude due to interference between signals emitted from the air-exposed and buried C8-PDI interfaces.

To assess the importance of spectral phase, we use this data as a target input for a series of calculations whose goal is to reproduce this data set starting from a randomly generated $\chi^{(2)}_{yzy}$ for each C8-PDI film interface. In one set of these calculations, which we label as direct fit, only the intensity of the target ESFG signal, $|\vec{E}_{samp}|^2$, is considered when fitting. In another, which we label as HD-ESFG fit, both the amplitude and phase of the target ESFG field are accounted for when fitting. The middle and bottom panels of Figure 8 display two representative fits to the target data set using these two methodologies, employing the same initial guess for the $\chi^{(2)}_{yzy}$ response of each C8-PDI film interface. Following optimization, both methodologies converge to fits that well reproduce the intensity of the ESFG field as a function of film thickness. We generally find this result to be true independent of the starting guess used for the $\chi^{(2)}_{yzy}$ response of each interface.

DOI: 10.1021/acs.jpcc.7b05514
J. Phys. Chem. C 2017, 121, 18653−18664

Interestingly, however, we find that the optimized $\chi^{(2)}_{yzy}$ response used for the buried interface strongly differs between the direct and HD-ESFG fits. Figure 9 compares the imaginary components of the optimized $\chi^{(2)}_{yzy}$ response found by each fitting routine. While both fits accurately reproduce the target $\chi^{(2)}_{yzy}$ of the air-exposed C8-PDI interface, the optimized response determined by direct fitting is unable to reproduce the $\chi^{(2)}_{yzy}$ of the buried surface, predicting that this line shape is composed of only a single Lorentzian resonance rather than a pair of peaks. In contrast, the HD-ESFG fit accurately reproduces the spectral position and amplitude of both peaks in the $\chi^{(2)}_{yzy}$ response of the buried C8-PDI interface, suggesting that the inclusion of spectral phase in our interference model can improve the accuracy of the line shapes for the $\chi^{(2)}$ tensor components recovered from it. While the calculation we highlight in Figure 9 is somewhat of an extreme case in that it yields completely different line shapes for the $\chi^{(2)}_{yzy}$ of the buried C8-PDI/SiO_2 interface, the improvement in the accuracy of recovering the buried $\chi^{(2)}_{yzy}$ line shape upon the inclusion of spectral phase holds across a range of different initial guesses for the $\chi^{(2)}_{yzy}$ of each interface and is somewhat insensitive to the algorithm used to optimize the fit. An expanded discussion of these results is given in the Supporting Information.

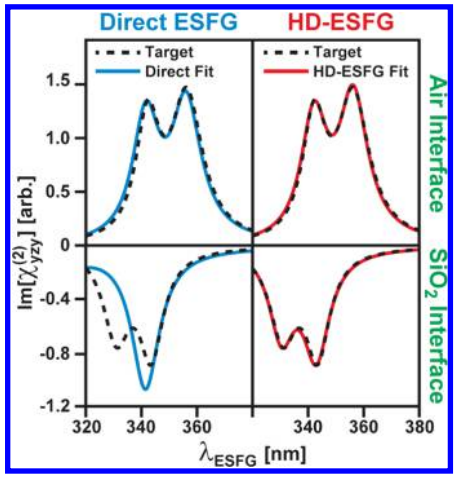

Figure 9. $\chi^{(2)}_{yzy}$ of air-exposed interface (top row) and C8-PDI/SiO_2 interface (bottom row) used to generate the target data in Figure 8 (black dashed lines) and reconstructions of this response obtained by fitting the target data with (right panels, red lines) and without (left panels, blue lines) accounting for the phase of the ESFG signal. While both direct and HD-ESFG fits in Figure 8 look very close to the target data, the HD-ESFG fit better reproduces the known target $\chi^{(2)}_{yzy}$ spectrum of the buried C8-PDI/SiO_2 interface.

We conclude that with the phase information we gain from HD-ESFG measurements, we can better determine the electronic DoS of C1-PDI molecules at buried interfaces. Our model calculations indicate that without accounting for the phase of the ESFG signal during interference modeling, we are in danger of retrieving an incorrect line shape for $\chi^{(2)}$ of the buried C1-PDI interface from these measurements. This can skew the interpretation of ESFG signals measured from these and other OSC films.

At present, we are in the process of applying a full interference modeling approach based on the phase-sensitive methodology outlined above to ESFG spectra recorded for both C1-PDI and C8-PDI thin films. Details regarding the results of this fitting are expansive enough that they merit a subsequent publication. However, in anticipation of this report, at present we can state that the features we observe in ESFG spectra of films of both materials deposited on SiO_2 suggest that they are subject to strain at the SiO_2 interface, which distorts their intermolecular arrangements from those preferred in the bulk of each material.

4. CONCLUSIONS AND OUTLOOK

In this report, we have demonstrated a simple method for incorporating heterodyne detection into a broadband ESFG spectrometer and described some of the benefits that HD-ESFG detection holds over the direct detection of ESFG signals, particularly for OSC thin films. HD-ESFG's sensitivity to low-amplitude signals can highlight weak features that appear in a spectrum. For samples such as OSC thin films that contain multiple ESFG-active layers, the phase information provided by HD-ESFG measurements can constrain optical models that seek to extract information on the electronic DoS of a specific interface within a sample. Without accounting for this phase, such interference models can be more prone to reporting spectra that do not accurately reflect the DoS of a buried interface. In addition, as the phase of an ESFG signal depends strongly on the thickness of a sample film, we believe that HD-ESFG measurements will be of great utility in the study of buried interfaces where the roughness of the buried surface cannot be ignored. The advantages mentioned above will be critical to both the implementation and interpretation of time-resolved ESFG studies, as they provide enhanced sensitivity to the electronic structure of buried interfaces while simultaneously reducing data collection times needed to record ESFG spectra.

■ ASSOCIATED CONTENT

Supporting Information

The Supporting Information is available free of charge on the ACS Publications website at DOI: 10.1021/acs.jpcc.7b05514.

Additional text, seven figures, and one table with expanded description of experimental layout for HD-ESFG measurements, solution absorption and emission spectra of C1-PDI, characterization of sample films by AFM and GIWAXS, scaling of direct ESFG and HD-ESFG signals with data collection time, potential for sample damage, and discussion of thin-film interference model used to produce results shown in Figures 8 and 9 (PDF)

■ AUTHOR INFORMATION

Corresponding Author

*E-mail roberts@cm.utexas.edu.

ORCID

Ravindra Pandey: 0000-0002-4396-9431

Sean T. Roberts: 0000-0002-3322-3687

Present Address

‡(R.P.) Department of Spectroscopy, Indian Association for the Cultivation of Science, Kolkata, India 700032.

Author Contributions

†A.P.M. and R.P. contributed equally to this manuscript.

Notes

The authors declare no competing financial interest.

DOI: 10.1021/acs.jpcc.7b05514
J. Phys. Chem. C 2017, 121, 18653−18664

■ ACKNOWLEDGMENTS

This work was supported by the American Chemical Society Petroleum Research Fund (Grant 55184-DN16), the Robert A. Welch Foundation (Grant F-1885), and a National Science Foundation Career Award (CHE-1654404). B.A.R. acknowledges support from an undergraduate research fellowship provided by the Office of the Vice President for Research at the University of Texas at Austin. We acknowledge the Texas Advanced Computing Center (TACC) at The University of Texas at Austin for providing computational resources in support of this work.

■ REFERENCES

(1) Smith, M. B.; Michl, J. Recent Advances in Singlet Fission. *Annu. Rev. Phys. Chem.* **2013**, *64*, 361.
(2) Wilson, M. W. B.; Rao, A.; Clark, J.; Kumar, R. S. S.; Brida, D.; Cerullo, G.; Friend, R. H. Ultrafast Dynamics of Exciton Fission in Polycrystalline Pentacene. *J. Am. Chem. Soc.* **2011**, *133*, 11830.
(3) Burdett, J. J.; Müller, A. M.; Gosztola, D.; Bardeen, C. J. Excited State Dynamics in Solid and Monomeric Tetracene: The Roles of Superradiance and Exciton Fission. *J. Chem. Phys.* **2010**, *133*, 144506.
(4) Eaton, S. W.; Shoer, L. E.; Karlen, S. D.; Dyar, S. M.; Margulies, E. A.; Veldkamp, B. S.; Ramanan, C.; Hartzler, D. A.; Savikhin, S.; Marks, T. J.; et al. Singlet Exciton Fission in Polycrystalline Thin Films of a Slip-Stacked Perylenediimide. *J. Am. Chem. Soc.* **2013**, *135*, 14701.
(5) Yost, S. R.; Lee, J.; Wilson, M. W. B.; Wu, T.; McMahon, D. P.; Parkhurst, R. R.; Thompson, N. J.; Congreve, D. N.; Rao, A.; Johnson, K.; et al. A Transferable Model for Singlet-Fission Kinetics. *Nat. Chem.* **2014**, *6*, 492.
(6) Monahan, N. R.; Sun, D.; Tamura, H.; Williams, K. W.; Xu, B.; Zhong, Y.; Kumar, B.; Nuckolls, C.; Harutyunyan, A. R.; Chen, G.; et al. Dynamics of the Triplet-Pair State Reveals the Likely Coexistence of Coherent and Incoherent Singlet Fission in Crystalline Hexacene. *Nat. Chem.* **2016**, *9*, 341.
(7) Le, A. K.; Bender, J. A.; Roberts, S. T. Slow Singlet Fission Observed in a Polycrystalline Perylenediimide Thin Film. *J. Phys. Chem. Lett.* **2016**, *7*, 4922.
(8) Margulies, E. A.; Logsdon, J. L.; Miller, C. E.; Ma, L.; Simonoff, E.; Young, R. M.; Schatz, G. C.; Wasielewski, M. R. Direct Observation of a Charge-Transfer State Preceding High-Yield Singlet Fission in Terrylenediimide Thin Films. *J. Am. Chem. Soc.* **2017**, *139*, 663.
(9) Sanders, S. N.; Kumarasamy, E.; Pun, A. B.; Steigerwald, M. L.; Sfeir, M. Y.; Campos, L. M. Singlet Fission in Polypentacene. *Chem.* **2016**, *1*, 505.
(10) Wang, C.; Tauber, M. J. High-Yield Singlet Fission in a Zeaxanthin Aggregate Observed by Picosecond Resonance Raman Spectroscopy. *J. Am. Chem. Soc.* **2010**, *132*, 13988.
(11) Korovina, N. V.; Das, S.; Nett, Z.; Feng, X.; Joy, J.; Haiges, R.; Krylov, A. I.; Bradforth, S. E.; Thompson, M. E. Singlet Fission in a Covalently Linked Cofacial Alkynyltetracene Dimer. *J. Am. Chem. Soc.* **2016**, *138*, 617.
(12) Hartnett, P. E.; Margulies, E. A.; Mauck, C. M.; Miller, S. A.; Wu, Y.; Wu, Y.-L.; Marks, T. J.; Wasielewski, M. R. Effects of Crystal Morphology on Singlet Exciton Fission in Diketopyrrolopyrrole Thin Films. *J. Phys. Chem. B* **2016**, *120*, 1357.
(13) Musser, A. J.; Maiuri, M.; Brida, D.; Cerullo, G.; Friend, R. H.; Clark, J. The Nature of Singlet Exciton Fission in Carotenoid Aggregates. *J. Am. Chem. Soc.* **2015**, *137*, 5130.
(14) Shockley, W.; Queisser, H. J. Detailed Balance Limit of Efficiency of P-N Junction Solar Cells. *J. Appl. Phys.* **1961**, *32*, 510.
(15) Hanna, M. C.; Nozik, A. J. Solar Conversion Efficiency of Photovoltaic and Photoelectrolysis Cells with Carrier Multiplication Absorbers. *J. Appl. Phys.* **2006**, *100*, 074510.
(16) Tayebjee, M. J. Y.; McCamey, D. R.; Schmidt, T. W. Beyond Shockley–Queisser: Molecular Approaches to High-Efficiency Photovoltaics. *J. Phys. Chem. Lett.* **2015**, *6*, 2367.
(17) Dexter, D. L. Two Ideas on Energy Transfer Phenomena: Ion-Pair Effects Involving the OH Stretching Mode, and Sensitization of Photovoltaic Cells. *J. Lumin.* **1979**, *18-19*, 779.
(18) Mongin, C.; Garakyaraghi, S.; Razgoniaeva, N.; Zamkov, M.; Castellano, F. N. Direct Observation of Triplet Energy Transfer from Semiconductor Nanocrystals. *Science* **2016**, *351*, 369.
(19) Huang, Z.; Li, X.; Mahboub, M.; Hanson, K. M.; Nichols, V. M.; Le, H.; Tang, M. L.; Bardeen, C. J. Hybrid Molecule–Nanocrystal Photon Upconversion Across the Visible and Near-Infrared. *Nano Lett.* **2015**, *15*, 5552.
(20) Tabachnyk, M.; Ehrler, B.; Gélinas, S.; Böhm, M. L.; Walker, B. J.; Musselman, K. P.; Greenham, N. C.; Friend, R. H.; Rao, A. Resonant Energy Transfer of Triplet Excitons from Pentacene to PbSe Nanocrystals. *Nat. Mater.* **2014**, *13*, 1033.
(21) Thompson, N. J.; Wilson, M. W. B.; Congreve, D. N.; Brown, P. R.; Scherer, J. M.; Bischof, T. S.; Wu, M.; Geva, N.; Welborn, M.; Voorhis, T. V.; et al. Energy Harvesting of Non-Emissive Triplet Excitons in Tetracene by Emissive PbS Nanocrystals. *Nat. Mater.* **2014**, *13*, 1039.
(22) Hayashi, T.; Castner, T. G.; Boyd, R. W. Quenching of Molecualr Fluorescence Near the Surface of a Semiconductor. *Chem. Phys. Lett.* **1983**, *94*, 461.
(23) Piland, G. B.; Burdett, J. J.; Hung, T.-Y.; Chen, P.-H.; Lin, C.-F.; Chiu, T.-L.; Lee, J.-H.; Bardeen, C. J. Dynamics of Molecular Excitons near a Semiconductor Surface Studied by Fluorescence Quenching of Polycrystalline Tetracene on Silicon. *Chem. Phys. Lett.* **2014**, *601*, 33.
(24) Yost, S. R.; Van Voorhis, T. Electrostatic Effects at Organic Semiconductor Interfaces: A Mechanism for "Cold" Exciton Breakup. *J. Phys. Chem. C* **2013**, *117*, 5617.
(25) Tersigni, A.; Shi, J.; Jiang, D. T.; Qin, X. R. Structure of Tetracene Films on Hydrogen-Passivated Si(001) Studied via STM, AFM, and NEXAFS. *Phys. Rev. B: Condens. Matter Mater. Phys.* **2006**, *74*, No. 205326.
(26) Jailaubekov, A. E.; Willard, A. P.; Tritsch, J. R.; Chan, W.-L.; Sai, N.; Gearba, R.; Kaake, L. G.; Williams, K. J.; Leung, K.; Rossky, P. J.; Zhu, X.-Y. Hot Charge-Transfer Excitons Set the Time Limit for Charge Separation at Donor/acceptor Interfaces in Organic Photovoltaics. *Nat. Mater.* **2013**, *12*, 66.
(27) Yi, Y.; Coropceanu, V.; Brédas, J.-L. Exciton-Dissociation and Charge-Recombination Processes in pentacene/C_{60} Solar Cells: Theoretical Insight into the Impact of Interface Geometry. *J. Am. Chem. Soc.* **2009**, *131*, 15777.
(28) Sai, N.; Gearba, R.; Dolocan, A.; Tritsch, J. R.; Chan, W.-L.; Chelikowsky, J. R.; Leung, K.; Zhu, X. Understanding the Interface Dipole of Copper Phthalocyanine (CuPc)/C_{60}: Theory and Experiment. *J. Phys. Chem. Lett.* **2012**, *3*, 2173.
(29) Zimmerman, J. D.; Xiao, X.; Renshaw, C. K.; Wang, S.; Diev, V. V.; Thompson, M. E.; Forrest, S. R. Independent Control of Bulk and Interfacial Morphologies of Small Molecular Weight Organic Heterojunction Solar Cells. *Nano Lett.* **2012**, *12*, 4366.
(30) Hestand, N. J.; Spano, F. C. Interference between Coulombic and CT-Mediated Couplings in Molecular Aggregates: H- to J-Aggregate Transformation in Perylene-Based π-Stacks. *J. Chem. Phys.* **2015**, *143*, 244707.
(31) Hestand, N. J.; Spano, F. C. Molecular Aggregate Photophysics beyond the Kasha Model: Novel Design Principles for Organic Materials. *Acc. Chem. Res.* **2017**, *50*, 341.
(32) Kazmaier, P. M.; Hoffmann, R. A Theoretical Study of Crystallochromy. Quantum Interference Effects in the Spectra of Perylene Pigments. *J. Am. Chem. Soc.* **1994**, *116*, 9684.
(33) Pandey, R.; Moon, A. P.; Bender, J. A.; Roberts, S. T. Extracting the Density of States of Copper Phthalocyanine at the SiO_2 Interface with Electronic Sum Frequency Generation. *J. Phys. Chem. Lett.* **2016**, *7*, 1060.
(34) Yamaguchi, S.; Tahara, T. Precise Electronic $\chi^{(2)}$ Spectra of Molecules Adsorbed at an Interface Measured by Multiplex Sum Frequency Generation. *J. Phys. Chem. B* **2004**, *108*, 19079.
(35) Yamaguchi, S.; Tahara, T. Determining Electronic Spectra at Interfaces by Electronic Sum Frequency Generation: One- and Two-

DOI: 10.1021/acs.jpcc.7b05514
J. Phys. Chem. C 2017, 121, 18653–18664

Photon Double Resonant Oxaxine 750 at the Air/water Interface. *J. Chem. Phys.* **2006**, *125*, 194711.
(36) Shen, Y. R. *The Principles of Nonlinear Optics*; Wiley–Interscience: New York, 1984.
(37) Shen, Y. R. Optical Second Harmonic Generation at Interfaces. *Annu. Rev. Phys. Chem.* **1989**, *40*, 327.
(38) Eisenthal, K. B. Equilibrium and Dynamic Processes at Interfaces by Second Harmonic and Sum Frequency Generation. *Annu. Rev. Phys. Chem.* **1992**, *43*, 627.
(39) Zhuang, X.; Miranda, P.; Kim, D.; Shen, Y. Mapping Molecular Orientation and Conformation at Interfaces by Surface Nonlinear Optics. *Phys. Rev. B: Condens. Matter Mater. Phys.* **1999**, *59*, 12632.
(40) Wang, H.-F.; Gan, W.; Lu, R.; Rao, Y.; Wu, B.-H. Quantitative Spectral and Orientational Analysis in Surface Sum Frequency Generation Vibrational Spectroscopy (SFG-VS). *Int. Rev. Phys. Chem.* **2005**, *24*, 191.
(41) Wilcox, D. E.; Lee, M. H.; Sykes, M. E.; Niedringhaus, A.; Geva, E.; Dunietz, B. D.; Shtein, M.; Ogilvie, J. P. Ultrafast Charge-Transfer Dynamics at the Boron Subphthalocyanine Chloride/C_{60} Heterojunction: Comparison between Experiment and Theory. *J. Phys. Chem. Lett.* **2015**, *6*, 569.
(42) Foglia, L.; Wolf, M.; Stähler, J. Ultrafast Dynamics in Solids Probed by Femtosecond Time-Resolved Broadband Electronic Sum Frequency Generation. *Appl. Phys. Lett.* **2016**, *109*, 202106.
(43) O'Brien, D. B.; Massari, A. M. Modeling Multilayer Thin Film Interference Effects in Interface-Specific Coherent Nonlinear Optical Spectroscopies. *J. Opt. Soc. Am. B* **2013**, *30*, 1503.
(44) O'Brien, D. B.; Massari, A. M. Experimental Evidence for an Optical Interference Model for Vibrational Sum Frequency Generation on Multilayer Organic Thin Film Systems I: Electric Dipole Approximation. *J. Chem. Phys.* **2015**, *142*, 024703.
(45) O'Brien, D. B.; Massari, A. M. Experimental Evidence for an Optical Interference Model for Vibrational Sum Frequency Generation on Multilayer Organic Thin Film Systems II: Consideration for Higher Order Terms. *J. Chem. Phys.* **2015**, *142*, 024704.
(46) O'Brien, D. B.; Massari, A. M. Simulated Vibrational Sum Frequency Generation from a Multilayer Thin Film System with Two Active Interfaces. *J. Chem. Phys.* **2013**, *138*, 154708.
(47) Kemnitz, K.; Bhattacharyya, K.; Hicks, J. M.; Pinto, G. R.; Eisenthal, K. B.; Heinz, T. F. The Phase of Second-Harmonic Light Generated at an Interface and Its Relation to Absolute Molecular Orientation. *Chem. Phys. Lett.* **1986**, *131*, 285.
(48) Yamaguchi, S.; Tahara, T. Heterodyne-Detected Electronic Sum Frequency Generation: "Up" versus "down" Alignment of Interfacial Molecules. *J. Chem. Phys.* **2008**, *129*, 101102.
(49) Nelson, C. A.; Luo, J.; Jen, A. K.-Y.; Laghumavarapu, R. B.; Huffaker, D. L.; Zhu, X.-Y. Time-, Energy-, and Phase-Resolved Second-Harmonic Generation at Semiconductor Interfaces. *J. Phys. Chem. C* **2014**, *118*, 27981.
(50) Park, H.; Gutierrez, M.; Wu, X.; Kim, W.; Zhu, X. Y. Optical Probe of Charge Separation at Organic/inorganic Semiconductor Interfaces. *J. Phys. Chem. C* **2013**, *117*, 10974.
(51) Stiopkin, I. V.; Jayathilake, H. D.; Bordenyuk, A. N.; Benderskii, A. V. Heterodyne-Detected Vibrational Sum Frequency Generation Spectroscopy. *J. Am. Chem. Soc.* **2008**, *130*, 2271.
(52) Wilson, P. T.; Jiang, Y.; Aktsipetrov, O. A.; Mishina, E. D.; Downer, M. C. Frequency-Domain Interferometric Second-Harmonic Spectroscopy. *Opt. Lett.* **1999**, *24*, 496.
(53) Chang, R. K.; Ducuing, J.; Bloembergen, N. Relative Phase Measurement between Fundamental and Second-Harmonic Light. *Phys. Rev. Lett.* **1965**, *15*, 6.
(54) Ostroverkhov, V.; Waychunas, G. A.; Shen, Y. R. New Information on Water Interfacial Structure Revelaed by Phase-Sensitive Surface Spectroscopy. *Phys. Rev. Lett.* **2005**, *94*, No. 046102.
(55) Pool, R. E.; Versluis, J.; Backus, E. H. G.; Bonn, M. Comparative Study of Direct and Phase-Specific Vibrational Sum-Frequency Generation Spectroscopy: Advantages and Limitations. *J. Phys. Chem. B* **2011**, *115*, 15362.
(56) Inoue, K.; Nihonyanagi, S.; Singh, P. C.; Yamaguchi, S.; Tahara, T. 2D Heterodyne-Detected Sum Frequency Generation Study on the Ultrafast Vibrational Dynamics of H_2O and HOD Water at Charged Interfaces. *J. Chem. Phys.* **2015**, *142*, No. 212431.
(57) Wilcox, D. E.; Sykes, M. E.; Niedringhaus, A.; Shtein, M.; Ogilvie, J. P. Heterodyne-Detected and Ultrafast Time-Resolved Second-Harmonic Generation for Sensitive Measurements of Charge Transfer. *Opt. Lett.* **2014**, *39*, 4274.
(58) Vanselous, H.; Petersen, P. B. Extending the Capabilities of Heterdoyne-Detected Sum-Frequency Generatino Spectroscopy: Probing Any Interface in Any Polarization Combination. *J. Phys. Chem. C* **2016**, *120*, 8175.
(59) Fu, L.; Chen, S.-L.; Wang, H.-F. Validation of Spectra and Phase in Sub-1 cm^{-1} Resolution Sum-Frequency Generation Vibrational Spectroscopy through Internal Heterodyne Phase-Resolved Measurement. *J. Phys. Chem. B* **2016**, *120*, 1579.
(60) Veenstra, K. J.; Petukhov, A. V.; De Boer, A. P.; Rasing, T. Phase-Sensitive Detection Technique for Surface Nonlinear Optics. *Phys. Rev. B: Condens. Matter Mater. Phys.* **1998**, *58*, R16020.
(61) Renaud, N.; Sherratt, P. A.; Ratner, M. A. Mapping the Relation between Stacking Geometries and Singlet Fission Yield in a Class of Organic Crystals. *J. Phys. Chem. Lett.* **2013**, *4*, 1065.
(62) Renaud, N.; Grozema, F. C. Intermolecular Vibration Modes Speed Up Singlet Fission in Perylenediimide Crystals. *J. Phys. Chem. Lett.* **2015**, *6*, 360.
(63) Xiong, W.; Laaser, J. E.; Mehlenbacher, R. D.; Zanni, M. T. Adding a Dimension to the Infrared Spectra of Interfaces Using Heterodyne Detected 2D Sum-Frequency Generation (HD 2D SFG) Spectroscopy. *Proc. Natl. Acad. Sci. U. S. A.* **2011**, *108*, 20902.
(64) Zhang, Z.; Piatkowski, L.; Bakker, H. J.; Bonn, M. Ultrafast Vibratinal Energy Transfer at the Water/Air Interface Revealed by Two-Dimensional. *Nat. Chem.* **2011**, *3*, 888.
(65) Inoue, K.; Ishiyama, T.; Nihonyanagi, S.; Yamaguchi, S.; Morita, A.; Tahara, T. Efficient Spectral Diffusion at the Air/Water Interface Revealed by Femtosecond Time-Resolved Heterodyne-Detected Vibrational Sum Frequency Generation Spectroscopy. *J. Phys. Chem. Lett.* **2016**, *7*, 1811.
(66) Mondal, S. K.; Yamaguchi, S.; Tahara, T. Molecules at the Air/water Interface Experience a More Inhomogeneous Solvation Environment than in Bulk Solvents: A Quantitative Band Shape Analysis of Interfacial Electronic Spectra Obtained by HD-ESFG. *J. Phys. Chem. C* **2011**, *115*, 3083.
(67) Kundu, A.; Yamaguchi, S.; Tahara, T. Evaluation of pH at Charged Lipid/Water Interfaces by Heterodyne-Detected Electronic Sum Frequency Generation. *J. Phys. Chem. Lett.* **2014**, *5*, 762.
(68) Yamaguchi, S.; Bhattacharyya, K.; Tahara, T. Acid–Base Equilibrium at an Aqueous Interface: pH Spectrometry by Heterodyne-Detected Electronic Sum Frequency Generation. *J. Phys. Chem. C* **2011**, *115*, 4168.
(69) Boyd, R. W. *Nonlinear Optics*; Academic Press: Boston, MA, 1992.
(70) Hadicke, E.; Graser, F. Structures of Eleven Perylene-3,4:9,10-Bis(dicarboximide) Pigments. *Acta Crystallogr., Sect. C: Cryst. Struct. Commun.* **1986**, *42*, 189.
(71) Hadicke, E.; Graser, F. Structures of Three Perylene-3,4:9,10-Bis(dicarboximide) Pigments. *Acta Crystallogr., Sect. C: Cryst. Struct. Commun.* **1986**, *42*, 195.
(72) Brixner, T.; Mancal, T.; Stiopkin, I. V.; Fleming, G. R. Phase-Stabilized Two-Dimensional Electronic Spectroscopy. *J. Chem. Phys.* **2004**, *121*, 4221.
(73) Rivera, C. A.; Bradforth, S. E.; Tempea, G. Gires-Tournois Interferometer Type Negative Dispersion Mirrors for Deep Ultraviolet Pulse Compression. *Opt. Express* **2010**, *18*, 18615.
(74) Dadap, J. I.; Shan, J.; Weling, A. S.; Misewich, J. A.; Heinz, T. F. Homodyne Detection of Second-Harmonic Generation as a Probe of Electric Fields. *Appl. Phys. B: Lasers Opt.* **1999**, *68*, 333.
(75) Moad, A. J.; Simpson, G. J. A Unified Treatment of Selection Rules and Symmetry Relations for Sum-Frequency and Second Harmonic Spectroscopies. *J. Phys. Chem. B* **2004**, *108*, 3548.

DOI: 10.1021/acs.jpcc.7b05514
J. Phys. Chem. C 2017, 121, 18653–18664

(76) Lin, C.-K.; Hayashi, M.; Lin, S. H. Theoretical Formulation and Simulation of Electronic Sum-Frequency Generation Spectroscopy. *J. Phys. Chem. C* **2013**, *117*, 23797.
(77) Klebe, G.; Graser, F.; Hädicke, E.; Berndt, J. Crystallochromy as a Solid-State Effect: Correlation of Molecular Conformation, Crystal Packing and Colour in Perylene-3,4:9,10-Bis(dicarboximide) Pigments. *Acta Crystallogr., Sect. B: Struct. Sci.* **1989**, *45*, 69.
(78) Schott AG. Optical Glass Data Sheets, 2015. www.us.schott.com/advanced_optics/english/download/index.html.

DOI: 10.1021/acs.jpcc.7b05514
J. Phys. Chem. C 2017, 121, 18653−18664